



Cite this: *RSC Adv.*, 2025, **15**, 29680

Redistribution of charge in a 2D/1D BiOBr/Bi₂O₂S heterojunction for the photoelectrocatalytic oxidation of organic pollutants in water

Kehinde D. Jayeola,^{ab} Dimpo S. Sipuka,^{ab} Tsholofelo I. Sebokolodi,^{ab} Jonathan O. Babalola,^{cd} Yumeng Zhao^e and Omotayo A. Arotiba^{ID *ab}

This study presents the design of a 2D/1D BiOBr/Bi₂O₂S p–n heterojunction developed for the degradation of organic pollutants in water, addressing the issue of water contamination caused by pharmaceutical compounds. In an *in situ* hydrothermal synthesis method, the BiOBr nanosheets were synthesised on Bi₂O₂S nanorods in varying ratio to form a heterojunction that maximises charge separation and suppressed charge recombination. At an optimal 20% Bi₂O₂S ratio, BiOBr/Bi₂O₂S heterojunction achieved 88% degradation efficiency of ciprofloxacin and TOC removal of 60%, when compared with the pristine BiOBr and Bi₂O₂S. The wider application of the photoanode was investigated by degrading other pollutants like tetracycline and sulfamethoxazole. Comprehensive structural, optical, and electrochemical analyses confirmed the increased surface area and active sites, enhanced light properties and better charged separation. The radical trapping studies identified the hydroxyl radical as a primary contributor to the degradation process, indication the p–n heterojunction facilitated by the formation of a space charge region. This study establishes the BiOBr/Bi₂O₂S as an effective photoanode for PEC water treatment and provides a promising approach to mitigate organic pollutant detection in water.

Received 29th May 2025
 Accepted 14th August 2025

DOI: 10.1039/d5ra03795f
rsc.li/rsc-advances

1. Introduction

The contamination of water by persistent organic pollutants including pharmaceuticals poses a severe threat to the environment and human health.^{1,2} Among several water treatment technologies, photoelectrochemical oxidation (PEC) has emerged to be a promising solution due to its ability to drive a complete mineralisation of pollutants under mild conditions with less production of toxic intermediates and by products.^{3–5} PEC system harnesses light and electrical energy to generate powerful oxidants for the degradation of pollutants in aqueous solution. In a typical PEC set up, the semiconductor photoanode absorbs light and generate charge carriers, then the photogenerated holes will migrate to the electrode surface, where they react with water molecules or hydroxyl ions to generate reactive oxygen species (ROS) like hydroxyl radicals, or even degrade pollutant directly.^{6,7} These ROS oxidise and break down organic pollutants in water into smaller molecules like

CO₂ and H₂O. Meanwhile, the photogenerated electrons migrates through the applied voltage/current to the cathode, where it indirectly takes part in the oxidation of the pollutant by reducing absorbed oxygen and converting it into superoxide anion radical.⁸

Moreover, recent advancements in PEC degradation process have been centred on the use of visible light active materials that can be activated with sunlight energy and has better stability for applicability and scalability purposes.⁹ Therefore, there has been a rise in exploring the properties of the two-dimension morphology in heterojunction formation.¹⁰ 2D semiconductors have gained attraction due to some unique properties. They possess high surface-area to volume ratio that can enhance light absorption and facilitates charge transfer, as thinner nanosheets have been reported to require shorter migration distance for charge carrier movement.^{11–13} An example is BiOBr nanosheet, which has layered structure, suitable band gap, and high chemical stability.¹⁴ In addition, BiOBr is a p-type semiconductor and possesses band gap energy ranging from 2.6–2.9 eV. However, BiOBr has drawbacks such as limited light absorption in the visible spectrum and relatively low charge mobility which affects its photoelectrocatalytic efficiency.¹⁵ An attempt to solve these challenges led to the formation of BiOBr based heterojunction. Semiconductor heterojunctions such as BiOBr/TiO₂,¹⁶ g-C₃N₄/BiOBr,¹⁷ WO₃/BiOBr,¹⁸ BiOBr/BiOI,¹⁹ BiOBr/Bi₂WO₆,²⁰ and so on have been

^aDepartment of Chemical Sciences, University of Johannesburg, Doornfontein Johannesburg, South Africa. E-mail: oarotiba@uj.ac.za

^bCentre for Nanomaterials Science Research, University of Johannesburg, South Africa

^cDepartment of Chemistry, University of Ibadan, Ibadan, Nigeria

^dBowen University, Iwo, Osun State, Nigeria

^eState Key Laboratory of Urban Water Resource and Environment, Harbin Institute of Technology, Harbin 150090, China



explored for photocatalysis and PEC water splitting, but the application of BiOBr based heterojunction is still limited for PEC water treatment.^{21,22}

On the other hand, $\text{Bi}_2\text{O}_2\text{S}$ is also a bismuth-based semiconductor with narrow band gap between 1.3–1.5 eV that facilitates absorption in the visible light region.^{23,24} It consists of a layered structure that promotes strong in-plane covalent bond and weak interlayer van der Waals interaction that helps to facilitate charge transport. $\text{Bi}_2\text{O}_2\text{S}$ exhibits high electron mobility, chemical stability and conductive active sites that assist in the effective degradation of pollutants.²⁵ Therefore, combining BiOBr and $\text{Bi}_2\text{O}_2\text{S}$ semiconductors to form a heterostructured photoanode will offer a better PEC water treatment system. The heterojunction formation BiOBr and $\text{Bi}_2\text{O}_2\text{S}$ semiconductors can create a favourable band alignment, which can potentially lead to a p–n junction configuration that can improve photoelectrochemical degradation efficiency.

In a p–n heterojunction, electron moves from the n-type semiconductor (excess electron) to the p-type semiconductor (excess holes) creating a negative charge on the surface of the p-type semiconductor and a positive charge on the n-type semiconductor, thus a depletion region at the interface. This electron diffusion continues until the Fermi level reaches equilibrium resulting in a space charge region at the p–n junction. When light is irradiated, both semiconductors will generate electrons and holes; however, the space charge region (built in electric field) will separate this by pushing the electrons to the n-type side and the holes to the p-type side. This separation of charges facilitates effective photoelectrochemical degradation process of pollutant^{19,26}

To interrogate the possible enhancement of PEC activity of the proposed BiOBr/ $\text{Bi}_2\text{O}_2\text{S}$ p–n heterojunction, we used ciprofloxacin, a commonly used fluoroquinolone antibiotics known for its effectiveness in treating various type of bacterial infections as a model pollutant.²⁷ Despite its efficacy as a drug, ciprofloxacin has become a significant environmental pollutant because of its persistence in water bodies, where it becomes resistant and accumulates over time. This persistence poses ecological risks including the development of antibiotic-resistant bacteria and adverse effect on aquatic bodies and humans' health.²⁸ Therefore, there is a need to generate efficient photoanode to remove ciprofloxacin from water. With the design of BiOBr based photoanode such as BiOBr/ $\text{Bi}_2\text{O}_2\text{S}$, we aim to explore the complementary electronic properties of each semiconductor for efficient charge transfer pathways leading to improved PEC performance. The synergistic combination of these semiconductors can be optimised to achieve better stability, light absorption and degradation efficiency.

Thus, this study is on the synthesis, structural properties, morphology, optical properties and charge transfer mechanism of 2D/1D BiOBr/ $\text{Bi}_2\text{O}_2\text{S}$ heterojunction photoanode for the PEC degradation of emerging contaminants in water. The choice of the pristine BiOBr is motivated by its inherent stability, layered structure and moderate band gap. In addition, BiOBr exhibits band gaps between 2.5–2.8 eV which allows for better visible light absorption and strong oxidation potential when compared with BiOCl ²⁹ and BiOI .³⁰ Although, BiOI possess band gaps

between 1.7–1.9 eV with strong visible light absorption abilities, it has weak redox capabilities. While $\text{Bi}_2\text{O}_2\text{S}$ was selected for its band structure and visible light absorption properties. To the best of our knowledge, this is the first study to report the fabrication, characterisation, and application of 2D/1D BiOBr/ $\text{Bi}_2\text{O}_2\text{S}$ heterojunction photoanode for PEC water treatment thus informing future efforts in designing heterojunction based photoanodes. Table 1 shows a comparative study with reported materials in literature to highlight that BiOBr/ $\text{Bi}_2\text{O}_2\text{S}$ is a promising material for water treatment.

2. Materials and METHODS

2.1. Materials used

Thiourea ($\text{CH}_4\text{N}_2\text{S}$), polyvinylidene fluoride (PVDF), lithium hydroxide monohydrate ($\text{LiOH H}_2\text{O}$), bismuth nitrate pentahydrate ($\text{Bi}(\text{NO}_3)_3 \cdot 5\text{H}_2\text{O}$), potassium bromide (KBr), acrylamide, water, potassium ferrocyanide ($\text{K}_4[\text{Fe}(\text{CN})_6]$), sodium sulphate (Na_2SO_4), *tert*-butanol, sodium ethylenediaminetetraacetate (EDTA), fluorine doped tin oxide glass, and *N*-methyl-2-pyrrolidone (NMP).

2.2. Photoanode preparation

2.2.1. Synthesis of BiOBr. The BiOBr nanosheets were synthesised using an hydrothermal method that was reported by Li *et al.*,⁴⁶ with slight modification. 0.002 moles of ($\text{Bi}(\text{NO}_3)_3 \cdot 5\text{H}_2\text{O}$) and 0.0021 mol of KBr is added into 50 mL of deionised water and sonicated for 30 min. The obtained mixture was then heated at 180 °C for 24 hours. The product was then cooled, washed with ethanol and deionised water several times, followed by drying for 8 hours.

2.2.2. Synthesis of $\text{Bi}_2\text{O}_2\text{S}$. The hydrothermal method of synthesis that was previously reported²³ was employed with slight modification for the preparation of $\text{Bi}_2\text{O}_2\text{S}$ nanorods. 0.004 moles of ($\text{Bi}(\text{NO}_3)_3 \cdot 5\text{H}_2\text{O}$) and 0.002 moles of $\text{CH}_4\text{N}_2\text{S}$ were dissolved in 40 mL of deionized water and sonicated for 20 min. then 0.28 moles of $\text{LiOH H}_2\text{O}$ were added and further sonicated for 60 min until a uniform reddish solution is formed. The solution was then transferred to crucible and placed in the furnace for 72 hours at 200 °C. After which the obtained product was washed thoroughly with ethanol and deionised severally and dried at 60 °C for 8 hours.

2.2.3. Synthesis of BiOBr/ $\text{Bi}_2\text{O}_2\text{S}$. For the BiOBr/ $\text{Bi}_2\text{O}_2\text{S}$ heterojunction, four mole ratios (5%, 10%, 20%, and 30%) of $\text{Bi}_2\text{O}_2\text{S}$ to BiOBr were synthesised *via in situ* hydrothermal method. The respective masses of the synthesised $\text{Bi}_2\text{O}_2\text{S}$ were dispersed in deionised water inside four different beakers. Each beaker containing 5%, 10%, 20%, and 30% of $\text{Bi}_2\text{O}_2\text{S}$ were sonicated for 30 min, followed by the synthesis of BiOBr as reported in Section 2.2.1.

2.2.4. Fabrication of photoanode. Drop-coating method was employed in the fabrication of BiOBr, $\text{Bi}_2\text{O}_2\text{S}$, and BiOBr/ $\text{Bi}_2\text{O}_2\text{S}$ photoanodes, on a fluorine doped tin oxide (FTO) glass substrate. A slurry paste formed from 50 mg of synthesised nanoparticles, 90 μL of *N*-methyl-2-pyrrolidone, and 5 mg of polyvinylidene fluoride was coated on the FTO glass using



Table 1 Reported materials for the photodegradation of organic pollutants

Semiconductors	Target analyte	Degradation efficiency, time	Reaction kinetics	Electrolyte	Ref.
FTO/NiSe ₂ /BiVO ₄	Ciprofloxacin	76%, 180 min	0.0065 min ⁻¹	Na ₂ SO ₄	31
Zr:BiVO ₄ @Bi ₂ S ₃ -CoS	Tetracycline hydrochloride	94%, 60 min	0.099 min ⁻¹	Na ₂ S/Na ₂ SO ₄	32
FTO/BiVO ₄ /BiOI	Ciprofloxacin	62%, 120 min	0.007 min ⁻¹	Na ₂ SO ₄	33
Bi ₂ WO ₆ -CNP-TiO ₂	Paracetamol	84%, 180 min	0.009 min ⁻¹	Na ₂ SO ₄	34
Fe/HNHC-PMS system	Bisphenol A	92.5%, 30 min	0.068 min ⁻¹	Not specified	35
CoNC/NHCNTs (PMS/photocatalysis)	Tetracycline	Close to 100%, 30 min	Not specified	—	36
WO ₃ /BiVO ₄	Di洛fenac	75–80%	Not specified	Na ₂ SO ₄	37
WO ₃ -g-C ₃ N ₄ /grafoil	Ciprofloxacin	75%, 75 min	0.004 min ⁻¹	Na ₂ SO ₄	38
BiOBr/BiO ₂ COOH (photocatalysis)	Levofloxacin	90.1%, 40 min	0.055 min ⁻¹	—	39
MgIn ₂ S ₄ /CeO ₂ (photocatalysis)	Tetracycline	86%, 120 min	0.027 min ⁻¹	—	40
rGO/BiOBr/TiO ₂	p-Chloronitrobenzene	86.8%, 360 min	0.005 min ⁻¹	—	41
Pt@CeO ₂ @MoS ₂ (PMS)	Carbamazepine	85%, 30 min	0.132 min ⁻¹	—	42
BiOBr@ZnIn ₂ S ₄ (photocatalysis)	Methyl orange	95%, 40 min	0.07 min ⁻¹	—	43
CuO/BiOCl	Aflatoxin B1	81.3%, 180 min	Not specified	—	44
Bi ₂ O ₂ S/NiTiO ₃	Sulfamethoxazole	80%, 180 min	0.008 min ⁻¹	Na ₂ SO ₄	45
BiOBr/Bi ₂ O ₂ S	Ciprofloxacin	88%, 180 min	0.0127 min ⁻¹	Na ₂ SO ₄	This work

a geometrical area of 1.7 cm by 1.7 cm. The coated FTO was then dried in the oven at 60 °C for 2 h.

2.3. Characterisation

The crystallinity and composition of the synthesised materials were performed using X-ray diffraction (XRD) (Cu K α radiation, Rigaku Ultima IV, Japan). The elemental composition and surface valence were analysed using X-ray photoelectron spectroscopy (XPS) and field-emission scanning electron microscope and Energy dispersive X-ray (FE-SEM-EDX) (JEOL JSM-7500F, Japan). The optical properties were examined using ultraviolet-visible diffuse reflectance spectrophotometry (UV-DRS) (Cary 60 UV-Vis, Malaysia). The recombination rate of photogenerated charge carriers was investigated using photoluminescence spectroscopy (PL) (F-186 2710, HITACHI, Japan). Surface morphologies of the semiconductors were investigated using transmission electron microscopy (TEM) (JOEL, Germany) and field-emission scanning electron microscope (FE-SEM) (JEOL JSM-7500F, Japan). The surface charge of the fabricated semiconductors was measured using the Zetasizer instrument (ZEECOM ZC 300, Japan). The degradation efficiency was monitored using UV-Vis spectroscopy (Cary 60 UV-Vis, Malaysia). The degradation pathway was monitored using ultra-performance liquid chromatography-mass spectrometry (UPLC-MS) (WATERs, USA). The surface area, pore size and pore volume were investigated using the Brunauer–Emmett–Teller (BET) analysis (Micrometrics Corporation ASAP 2020 V4.00). The effect of temperature on the synthesis semiconductors were investigated using the thermogravimetric analysis (TGA Q500, TA Instruments, USA).

The photodegradation measurement and degradation procedure are presented in Section S1 of the SI section.

3. Results and discussions

3.1. Structural, surface, and morphology studies

Fig. 1a shows XRD diffraction pattern of the synthesised BiOBr, Bi₂O₂S, and BiOBr/Bi₂O₂S. The major peaks of BiOBr at the 2

theta 10.77°, 21.77°, 25.08°, 31.55°, 32.14°, 39.20°, 46.14°, 50.66°, & 57.07 are indexed to the *hkl* (001), (002), (101), (102), (110), (112), (200), (104) and (212) planes of the BiOBr tetragonal phase (JCPDS #00-009-0393).⁴⁷ On the other hand, the peaks of Bi₂O₂S at 2 theta 27.18°, 29.53°, 31.81°, 32.78°, 46.2°, 48.80°, 54.21°, 55.62°, & 57.83° are indexed to the *hkl* (120), (040), (130), (101), (060), (002), (112), (221), and (161) planes of Bi₂O₂S orthorhombic phase (JCPDS #01-085-0451).⁴⁸ The diffraction pattern of BiOBr/Bi₂O₂S show peaks at 2 theta 10.77°, 21.77°, 25.08°, 31.70°, 32.14°, 39.20°, 46.2°, 56.13°, & 57.14° corresponds to the main peaks of BiOBr and Bi₂O₂S. Peaks overlaps which led to a peak broadening are observed at 2 theta 31.70° and 32.14° which corresponds to the *hkl* (130) & (101) and (102) & (110) plane of Bi₂O₂S and BiOBr respectively, thus confirming the formation of heterojunction.

The FESEM micrograph of BiOBr (Fig. S1) shows a layered sheet-like structure with a two-dimension (2D) morphology. The nanosheet appeared to be thin, flat and well distributed, forming an interconnected structure. The FESEM micrograph of Bi₂O₂S (Fig. S2) reveals a rod-like, one-dimensional (1D) morphology, that displayed a high aspect ratio with elongated structures which are uniformly distributed and interconnected. FESEM micrograph of BiOBr/Bi₂O₂S (Fig. 1b) shows the combination of the rod-like and sheet-like structure of Bi₂O₂S and BiOBr respectively. The rods appeared to be intertwined within the flatter nanosheets, leading to increased surface area and active sites for photoelectrochemical degradation. Furthermore, the TEM micrograph BiOBr (Fig. 1c) confirms the interconnected sheet-like structure. Also, the TEM micrograph of Bi₂O₂S (Fig. 1d) confirms the elongated rod-like morphology, with rough edges and texture. And, the TEM micrograph of BiOBr/Bi₂O₂S (Fig. 1e) shows the intertwined and interconnected pattern of BiOBr nanosheet and Bi₂O₂S nanorod. The combination of nanosheet and nanorod structure in the heterojunction photoanode led to an increase in degradation efficiency due to improved charge separation and increased light absorption properties of the unique morphologies.



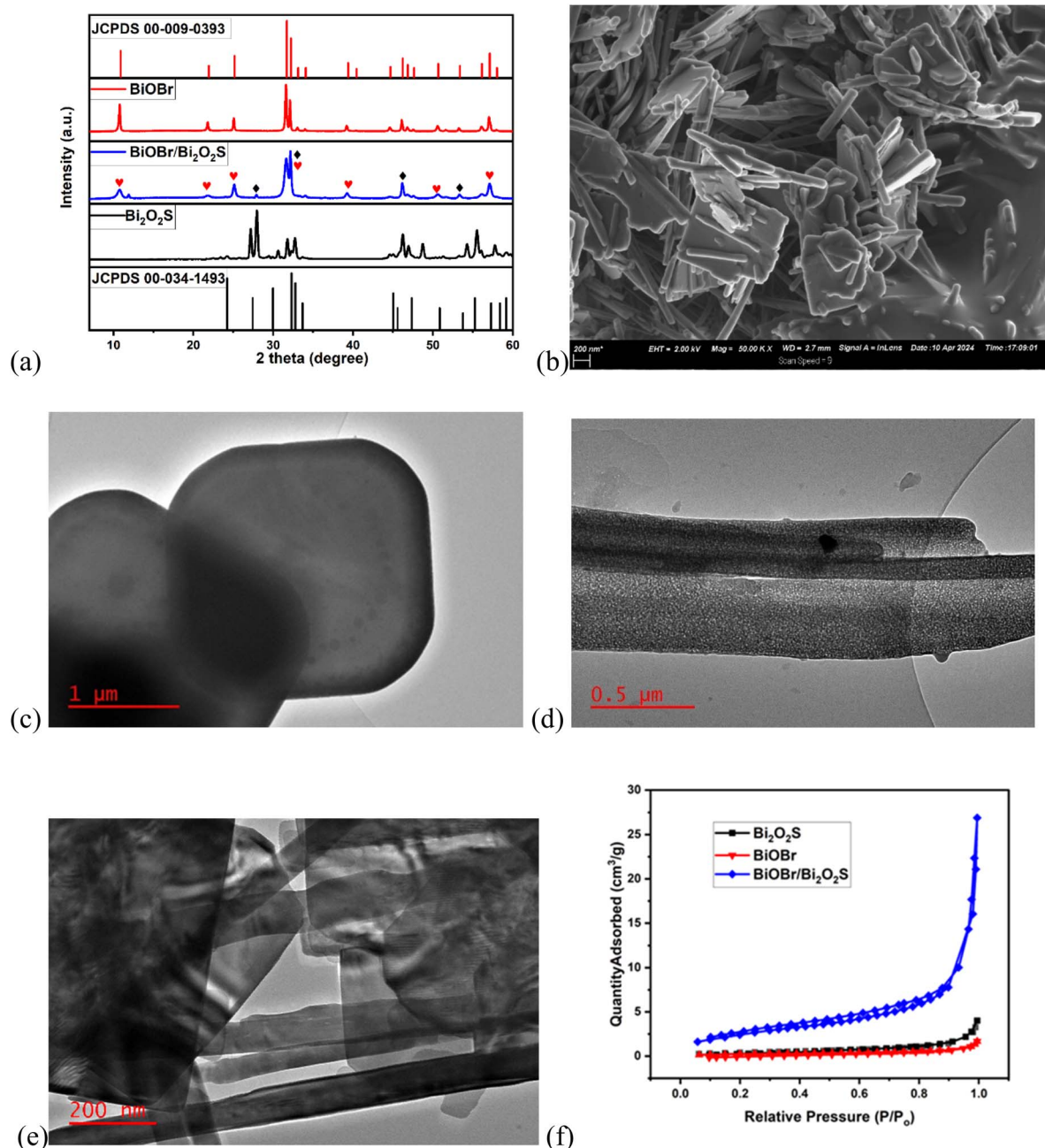


Fig. 1 (a) XRD pattern of BiOBr, Bi₂O₂S and BiOBr/Bi₂O₂S (b) FESEM micrograph of BiOBr/Bi₂O₂S. TEM micrograph (c) BiOBr, (d) Bi₂O₂S, (e) BiOBr/Bi₂O₂S. (f) BET Isotherm curve of BiOBr, Bi₂O₂S and BiOBr/Bi₂O₂S.

The N₂ adsorption-desorption isotherm curve of BiOBr, Bi₂O₂S, & BiOBr/Bi₂O₂S (Fig. 1f) shows hysteresis loops that are often observed in Type IV isotherms. This type of isotherm is characteristics of mesoporous materials. The Brunauer–Emmett–Teller (BET) and Barrett–Joyner–Halenda (BJH) analyses were used to estimate the surface area and pore volume respectively, of BiOBr, Bi₂O₂S, & BiOBr/Bi₂O₂S. The surface area of 0.958 m² g⁻¹, 1.581 m² g⁻¹, & 9.4045 m² g⁻¹ were calculated for BiOBr, Bi₂O₂S, and BiOBr/Bi₂O₂S respectively, with the corresponding pore volume of 0.0025 cm³ g⁻¹, 0.0062 cm³ g⁻¹, & 0.4160 cm³ g⁻¹. Therefore, the heterojunction formation led to

increased surface area and pore volume, which are useful for efficient light harvesting.⁴⁹

The FTIR spectra of BiOBr, Bi₂O₂S, and BiOBr/Bi₂O₂S (Fig. S3) reveal the functional groups that are present. For BiOBr spectra, the peak at 3458 cm⁻¹ and 1639 cm⁻¹ can be ascribed to the O–H stretching and bending vibrations due to absorbed water. The peaks at 2033 cm⁻¹ and 1415 cm⁻¹ can be attributed to C–O stretching and bending vibrations due to absorbed atmospheric CO₂. These peaks are mostly associated with samples prepared using KBr. While, the peak positioned at 1275 cm⁻¹ and 523 cm⁻¹ are attributed to stretching vibration

of Bi–O bonds associated with halogenated bismuth compounds.⁵⁰ The absorption bands of $\text{Bi}_2\text{O}_2\text{S}$ at 1420 cm^{-1} corresponds to the S–O bending vibration. And, the peaks at 867 cm^{-1} & 484 cm^{-1} correspond to Bi–O stretching and bending vibration, respectively.²³ All these characteristic peaks of BiOBr and $\text{Bi}_2\text{O}_2\text{S}$ were observed in the spectra of BiOBr/ $\text{Bi}_2\text{O}_2\text{S}$ with an appearance of a new peak at 607 cm^{-1} . The appearance of this peak suggests a possible modification around the Bi–O and S–O bonds due to heterojunction formation.⁵¹

3.2. Elemental composition

The XPS survey scans of BiOBr, $\text{Bi}_2\text{O}_2\text{S}$ and BiOBr/ $\text{Bi}_2\text{O}_2\text{S}$ (Fig. 2a) reveal the presence of the bismuth, sulphur, oxygen, and bromine. The O 1s spectra (Fig. 2b) show peaks with binding energy of 529.4 eV , 530.8 eV & 532.3 eV for $\text{Bi}_2\text{O}_2\text{S}$ which correspond to the lattice (Bi–O), chemisorbed, and physically absorbed oxygen, while the peaks at 530.2 eV , and 531.4 eV observed for BiOBr corresponds to the lattice (Bi–O) and chemisorbed oxygen. The positive shift in binding energy of 530.5 eV , 531.8 eV , and 533.5 eV observed for BiOBr/ $\text{Bi}_2\text{O}_2\text{S}$ for the lattice, chemisorbed, and physically absorbed oxygen is due to the increased interaction of the metal–oxygen bonds in BiOBr and $\text{Bi}_2\text{O}_2\text{S}$, resulting from heterojunction formation.

Additionally, the Bi 4f spectra (Fig. 2c) reveals the Bi 4f peaks at 158.6 eV and 163.9 eV for $\text{Bi}_2\text{O}_2\text{S}$, and at 159.2 eV and 164.6 eV for BiOBr. These peaks shifted to 159.5 eV and 164.8 eV in BiOBr/ $\text{Bi}_2\text{O}_2\text{S}$ corresponds to Bi 4f_{7/2} and Bi 4f_{5/2} respectively. The S 2p orbital peak was observed at 169 eV for $\text{Bi}_2\text{O}_2\text{S}$, although it was absent in the BiOBr/ $\text{Bi}_2\text{O}_2\text{S}$ spectra. This could be due to the low percentage of sulphur in the composite thus falling below the detection limit of XPS. Moreover, the FESEM-EDX spectra (Fig. S4) confirmed the presence of bismuth, bromide, oxygen, as well as sulphur in the BiOBr/ $\text{Bi}_2\text{O}_2\text{S}$ heterojunction, where sulphur is detected in a low percentage of 0.3% . Furthermore, the Br 3d spectra shows peak at 68.5 eV of BiOBr, which shifted to 69.1 eV in BiOBr/ $\text{Bi}_2\text{O}_2\text{S}$. These shifts to a higher binding energy of the orbitals of both BiOBr and $\text{Bi}_2\text{O}_2\text{S}$ indicate a change in electron density which causes a redistribution of charges across the interface of the semiconductor.⁵² This could suggest that the electronic interaction between BiOBr and $\text{Bi}_2\text{O}_2\text{S}$ facilitated charge separation to promote charge mobility.

3.3. Photo(electro)chemical properties

As shown in Fig. 3a, the photocurrent densities of BiOBr, $\text{Bi}_2\text{O}_2\text{S}$, BiOBr/5% $\text{Bi}_2\text{O}_2\text{S}$, BiOBr/10% $\text{Bi}_2\text{O}_2\text{S}$, BiOBr/20% $\text{Bi}_2\text{O}_2\text{S}$, & BiOBr/30% $\text{Bi}_2\text{O}_2\text{S}$ photoanodes were deduced as

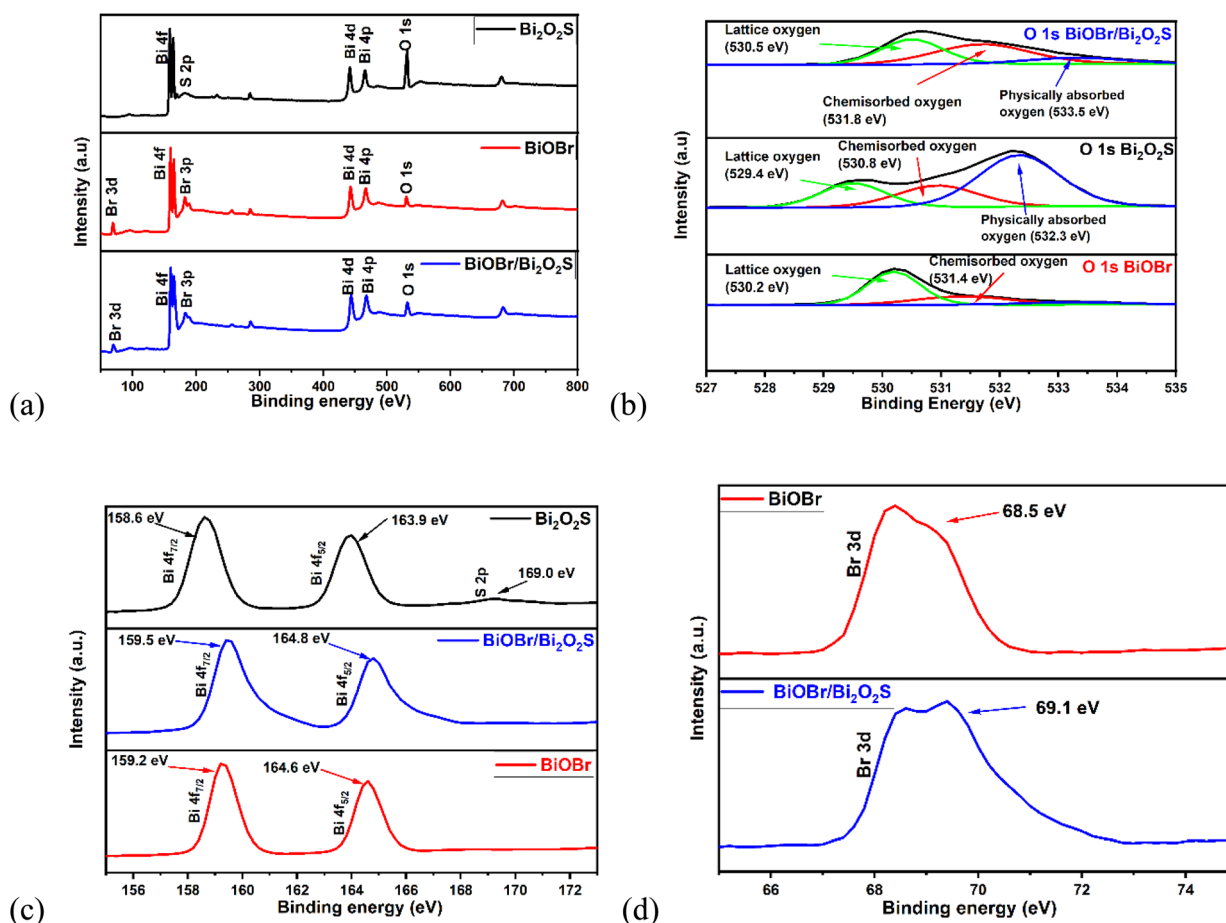


Fig. 2 (a) XPS survey scan. XPS spectra of (b) O 1s, (c) Bi 4f and S 2p, of BiOBr, $\text{Bi}_2\text{O}_2\text{S}$ and BiOBr/ $\text{Bi}_2\text{O}_2\text{S}$. (d) Br 3d of BiOBr and BiOBr/ $\text{Bi}_2\text{O}_2\text{S}$

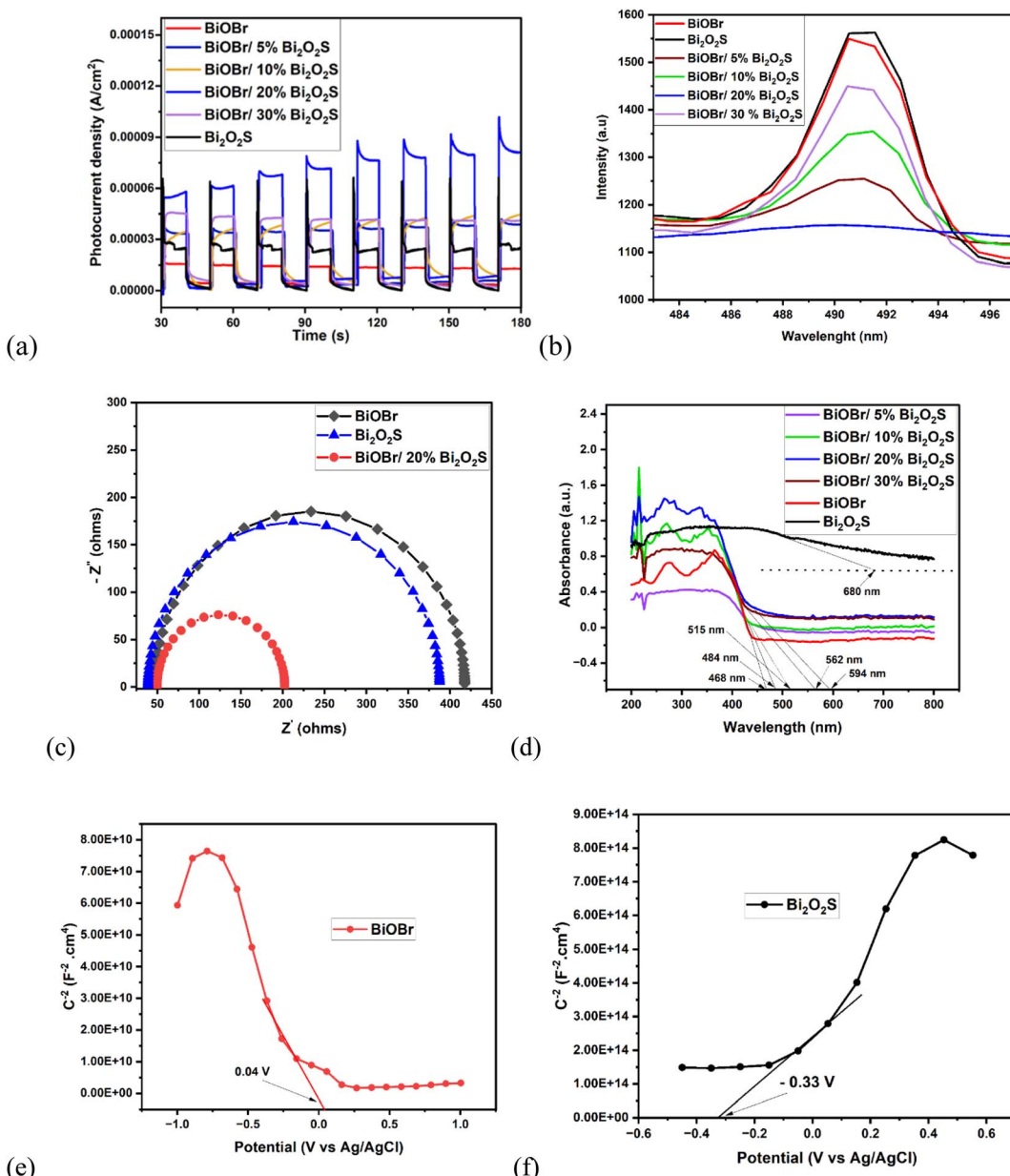


Fig. 3 (a) Transient photocurrent response plot, (b) photoluminescence spectra, of BiOBr, Bi₂O₂S, BiOBr/5% Bi₂O₂S, BiOBr/10% Bi₂O₂S, BiOBr/20% Bi₂O₂S, & BiOBr/30% Bi₂O₂S. (c) EIS Nyquist plot BiOBr, Bi₂O₂S, & BiOBr/Bi₂O₂S, (d) UV-Vis DRS spectra of BiOBr, Bi₂O₂S, BiOBr/5% Bi₂O₂S, BiOBr/10% Bi₂O₂S, BiOBr/20% Bi₂O₂S, & BiOBr/30% Bi₂O₂S. Mott Schottky curve of (e) BiOBr, (f) Bi₂O₂S

0.015 mA cm⁻², 0.065 mA cm⁻², 0.030 mA cm⁻², 0.037 mA cm⁻², 0.212 mA cm⁻², and 0.041 mA cm⁻² respectively. Amongst the four different mole ratios, the BiOBr/20% Bi₂O₂S gave the highest densities which is 14 times greater than the photocurrent density of BiOBr and 3 times greater than that of Bi₂O₂S. This suggests that the BiOBr/20% Bi₂O₂S is more capable of light harvesting, efficient charge separation and better degradation efficiency.

Likewise, the photoluminescence spectra (Fig. 3b) reveal that the rate of recombination of photogenerated holes and electrons were more suppressed in the BiOBr/20% Bi₂O₂S heterojunction when compared to BiOBr/5% Bi₂O₂S, BiOBr/10%

Bi₂O₂S, and BiOBr/30% Bi₂O₂S. A lower PL intensity suggests a lower or suppressed recombination rate of charge carriers.²³ Moreover, the charge transfer resistance of the photoanodes using the EIS Nyquist plot (Fig. 3c) were found to be 372 Ω, 353 Ω, and 153 Ω for BiOBr, Bi₂O₂S, and BiOBr/20% Bi₂O₂S respectively. This suggests that BiOBr/Bi₂O₂S exhibits improved charge transfer efficiency with lower resistance of electron mobility which contributes to its superior performance in the PEC degradation process.

Also, the light absorption properties of the photoanodes were investigated using the UV-Vis DRS. As displayed in Fig. 3d, the pristine BiOBr has an absorption edge of 468 nm, indicating



a wider band gap which limits its light absorption to the UV region, while $\text{Bi}_2\text{O}_2\text{S}$ has an absorption edge of 680 nm, indicating a narrow band gap which allows for absorption in a broader spectrum of the visible light. $\text{BiOBr}/5\% \text{Bi}_2\text{O}_2\text{S}$, $\text{BiOBr}/10\% \text{Bi}_2\text{O}_2\text{S}$, $\text{BiOBr}/15\% \text{Bi}_2\text{O}_2\text{S}$ and $\text{BiOBr}/30\% \text{Bi}_2\text{O}_2\text{S}$ gave absorption edge of 484 nm, 515 nm, 562 nm, & 594 nm respectively. This implies that the increase in the mole ratio of $\text{Bi}_2\text{O}_2\text{S}$ to BiOBr in the heterojunction lead to increase in narrowing of $\text{BiOBr}/\text{Bi}_2\text{O}_2\text{S}$ heterojunction band gap.

3.4. Band energies calculation

Using eqn (1), the band gap energy of BiOBr (Fig. S5) and $\text{Bi}_2\text{O}_2\text{S}$ (Fig. S6) were deduced to be 2.61 eV and 1.32 eV respectively.

$$\varepsilon h\nu = C(h\nu - E_g)^n \quad (1)$$

C is the constant, n is determined by the type of transition, E_g is the band gap energy, and $h\nu$ is the incident photon energy.

Also, the conduction and valence band energies were calculated based on vacuum scale and electronegativity using eqn (2) and (3).

$$E_{\text{CB}} = X - E_{\text{C}} - 0.5 E_g \quad (2)$$

$$E_{\text{CB}} = E_{\text{VB}} - E_g \quad (3)$$

E_{VB} = valence band, E_{CB} = conduction band, E_{C} = energy of free electrons (4.5 eV), X = Mulliken electronegativity, and E_g = band gap energy.

The X values for BiOBr and $\text{Bi}_2\text{O}_2\text{S}$ were calculated to be 6.17 eV (ref. 53) and 4.81 eV (ref. 48) respectively. Therefore, the $E_{\text{CB}(\text{NHE})}$ of BiOBr and $\text{Bi}_2\text{O}_2\text{S}$ are +0.37 eV and -0.34 eV with the corresponding $E_{\text{VB}(\text{NHE})}$ of 2.96 eV and 0.94 eV, respectively.

The negative and positive slope observed in the Mott Schottky curve of BiOBr (Fig. 3e) and $\text{Bi}_2\text{O}_2\text{S}$ (Fig. 3f) confirmed that BiOBr is a p-type semiconductor, while $\text{Bi}_2\text{O}_2\text{S}$ is a n-type semiconductor. Moreover, the flat band potentials (E_f) were deduced with respect to Ag/AgCl electrode. The E_f values of +0.04 and -0.33 V were obtained for BiOBr and $\text{Bi}_2\text{O}_2\text{S}$ respectively. From eqn (4), the E_f was calculated with respect to the normal hydrogen electrode. Hence, the $E_{f(\text{NHE})}$ approximately is 0.23 eV and -0.13 eV which is related to the Fermi level position with respect to the conduction band of BiOBr and $\text{Bi}_2\text{O}_2\text{S}$ respectively.

$$E_{(\text{NHE})} = E_{(\text{Ag}/\text{AgCl})} + 0.194 \quad (4)$$

In addition, the XPS valence spectra was used to calculate the $E_{\text{VB}(\text{XPS})}$ which is with respect to the Fermi level. The valence band maxima (VBM) of 2.57 eV and 0.54 eV were deduced for BiOBr (Fig. S7) and $\text{Bi}_2\text{O}_2\text{S}$ (Fig. S8) respectively. The relationship between the $E_{\text{VB}(\text{NHE})}$ and $E_{\text{VB}(\text{XPS})}$ is shown in eqn (5).⁵⁴

$$E_{\text{VB},\text{NHE}} = \phi + E_{\text{VB},\text{XPS}} - 4.44 \quad (5)$$

where, the work function (ϕ) of the XPS instrument is given as 4.8 eV.

Therefore, the expected $E_{\text{VB}(\text{NHE})}$ for BiOBr and $\text{Bi}_2\text{O}_2\text{S}$ are 2.93 eV and 0.90 eV respectively. These values agree with the calculated $E_{\text{VB}(\text{NHE})}$ with a difference of less than 0.1.

3.5. Photoelectrochemical degradation

3.5.1. Effect of heterojunction, pH, analytes and TOC studies. Ciprofloxacin was selected as the targeted organic pollutant to investigate the photoelectrocatalytic efficiency of the fabricated $\text{BiOBr}/\text{Bi}_2\text{O}_2\text{S}$ heterojunction. $\text{BiOBr}/20\% \text{Bi}_2\text{O}_2\text{S}$ gave the highest degradation efficiency of 88% of CIP after 180 min, when compared to BiOBr , $\text{Bi}_2\text{O}_2\text{S}$, $\text{BiOBr}/5\% \text{Bi}_2\text{O}_2\text{S}$, $\text{BiOBr}/10\% \text{Bi}_2\text{O}_2\text{S}$, & $\text{BiOBr}/30\% \text{Bi}_2\text{O}_2\text{S}$ which gave 49%, 63%, 82%, 70% and 72% respectively (Fig. 4a). This shows that the $\text{BiOBr}/20\% \text{Bi}_2\text{O}_2\text{S}$ heterojunction demonstrated enhanced degradation performance over the pristine BiOBr and $\text{Bi}_2\text{O}_2\text{S}$. Therefore, the 20% $\text{Bi}_2\text{O}_2\text{S}$ was used as the optimised heterojunction ratio. In addition, the data obtained were fitted linearly using the pseudo first order reaction model to obtain the rate of reaction. As displayed in Fig. S9, the k values obtained for BiOBr , $\text{Bi}_2\text{O}_2\text{S}$ & $\text{BiOBr}/20\% \text{Bi}_2\text{O}_2\text{S}$ are 0.0036 min^{-1} , 0.0059 min^{-1} , and 0.0131 min^{-1} respectively. This shows that the formation of heterojunction led to a faster rate of reaction.

The effect of current density on the degradation efficiency of $\text{BiOBr}/20\% \text{Bi}_2\text{O}_2\text{S}$ was also investigated. The current density varied from 2 mA cm^{-2} to 7 mA cm^{-2} (Fig. 4b), at 2 mA cm^{-2} , the lowest degradation efficiency of 49% was observed. While 5 mA cm^{-2} & 7 mA cm^{-2} gave 88% & 89% respectively. However, since current generated is related to energy consumption, the optimal current density of 5 mA cm^{-2} was used for this study. Moreover, the effect of current density was also investigated for the pristine BiOBr & $\text{Bi}_2\text{O}_2\text{S}$ to show the effect of heterojunction formation. As shown in Fig. S10 for BiOBr , degradation efficiency of 37%, 49%, & 53% and for $\text{Bi}_2\text{O}_2\text{S}$ (Fig. S11), degradation efficiency of 27%, 63% & 35% were observed for 2 mA cm^{-2} , 5 mA cm^{-2} & 7 mA cm^{-2} respectively. This shows that BiOBr & $\text{Bi}_2\text{O}_2\text{S}$ yield a lower degradation efficiency when compared with $\text{BiOBr}/\text{Bi}_2\text{O}_2\text{S}$. And at 7 mA cm^{-2} , $\text{Bi}_2\text{O}_2\text{S}$ electrode experienced leaching showing that it unstable after 60 min.

In addition, the efficiency of the $\text{BiOBr}/\text{Bi}_2\text{O}_2\text{S}$ photoanode in different environments were investigated using CIP solution at different pH and two other organic pollutants (sulfamethoxazole and tetracycline). At pH 3, pH 7, and pH 10 of CIP solutions, degradation efficiencies of 71%, 88%, & 71% were recorded (Fig. 4c) where the pH of 7 gave the highest degradation efficiency. Ciprofloxacin has two pK_a s values of 6.09 (carboxylic group is deprotonated) and 8.62 (the amino group is deprotonated).⁵⁵ This implies that at pH 3 and pH 10, CIP will exist primarily in its cationic and anionic form respectively which might not be favourable due to electrostatic repulsion, thus in the zwitterionic form at pH 7, electrostatic reaction can be enhanced, thus leading to enhanced degradation efficiency. Also, the degradation efficiency of sulfamethoxazole (pH 6.7) and tetracycline (pH 7) gave 71% and 63% respectively (Fig. 4c). Although, the three analytes degraded in the similar pH but gave different results. This suggests that the simplicity of



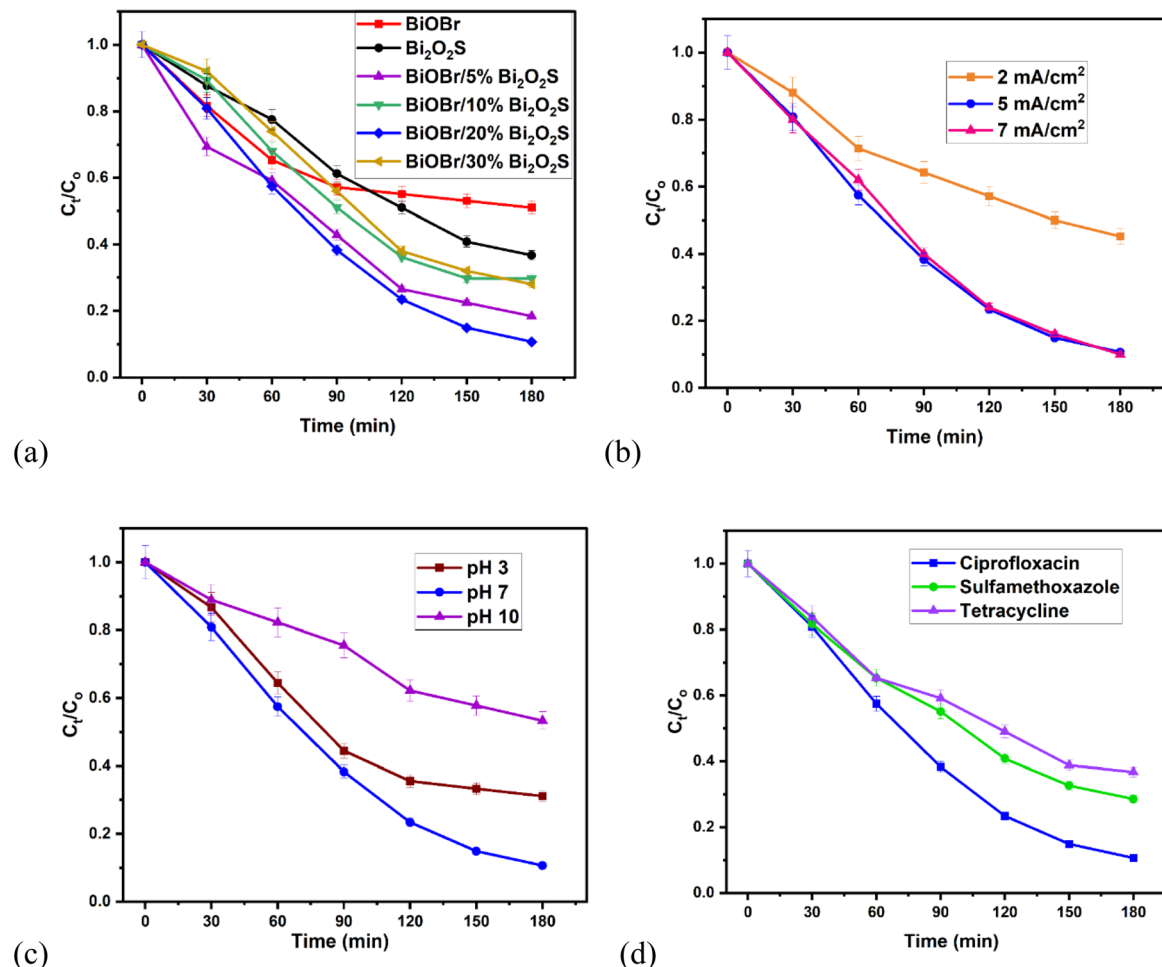


Fig. 4 The PEC degradation efficiency plot showing (a) effect of heterojunction, (b) effect of current density, (c) effect of pH, (d) different analyte study (experimental conditions: ciprofloxacin concentration = 5 mg L⁻¹ in 0.1 M Na₂SO₄, current density = 5 mA cm⁻²)

complexity of the structure of the analyte is one of the factors that can affect the degradation efficiency of a photoanode.

The total organic carbon (TOC) percentage removal of ciprofloxacin using BiOBr/Bi₂O₃S photoanode was investigated. As shown in Fig. S12, the initial TOC concentration was 30.5 ppm, and after degradation, the final TOC was 12.21 ppm. From eqn (6), the TOC removal was found to be 60%.

$$\% \text{ Removal} = \frac{\text{TOC}_t - \text{TOC}_0}{\text{TOC}_t} \times 100 \quad (6)$$

where TOC_t = final total organic carbon concentration (ppm), TOC = initial total organic carbon concentration (ppm).

Therefore, the heterojunction of BiOBr and Bi₂O₃S resulted in better photoelectrocatalytic activity, which is attributed to effective charge transfer and separation.

3.5.2. Synergy and kinetics studies. The synergistic effect of the electrochemical oxidation (EC) and photocatalysis (PC) processes were investigated. PEC degradation of ciprofloxacin over BiOBr/Bi₂O₃S photoanode gave the highest degradation efficiency when compared to EC (48%), and PC (18%), and photolysis (16%) processes (Fig. 5a). This explains the synergistic effect of the electrochemical oxidation and photocatalysis

processes involved in PEC degradation process are responsible for the enhanced PEC degradation efficiency. Therefore, PEC offers the most effective degradation route due to the combined effect of light and electrical energy which enhances reactive species generation. In addition, the data obtained were fitted linearly using the pseudo first order reaction model to obtain the rate of reaction involved in these processes. As displayed in Fig. 5b, the k values obtained for PEC, EC, PC, and photolysis are 0.0127 min⁻¹, 0.0037 min⁻¹, 0.0011 min⁻¹, and 0.004 min⁻¹ respectively. This shows that the fastest rate of reaction was observed in PEC. Furthermore, the synergistic factor (SF) of 1.44 was calculated from eqn (7).

$$\text{SF} = \frac{K_{\text{PEC}}}{K_{\text{PC}} + K_{\text{EC}} + K_{\text{PHOTO}}} - 1 \quad (7)$$

3.5.3. Reusability experiment and radical determination. The stability and reusability of BiOBr/Bi₂O₃S photoanode were tested through a 7-cycle of degradation of ciprofloxacin (Fig. 5c). The difference of approximately 1% was observed in the first 5 cycles, then by the 6th cycle, the degradation efficiency had reduced from 88% to 81%. And, by the 7th cycle, the



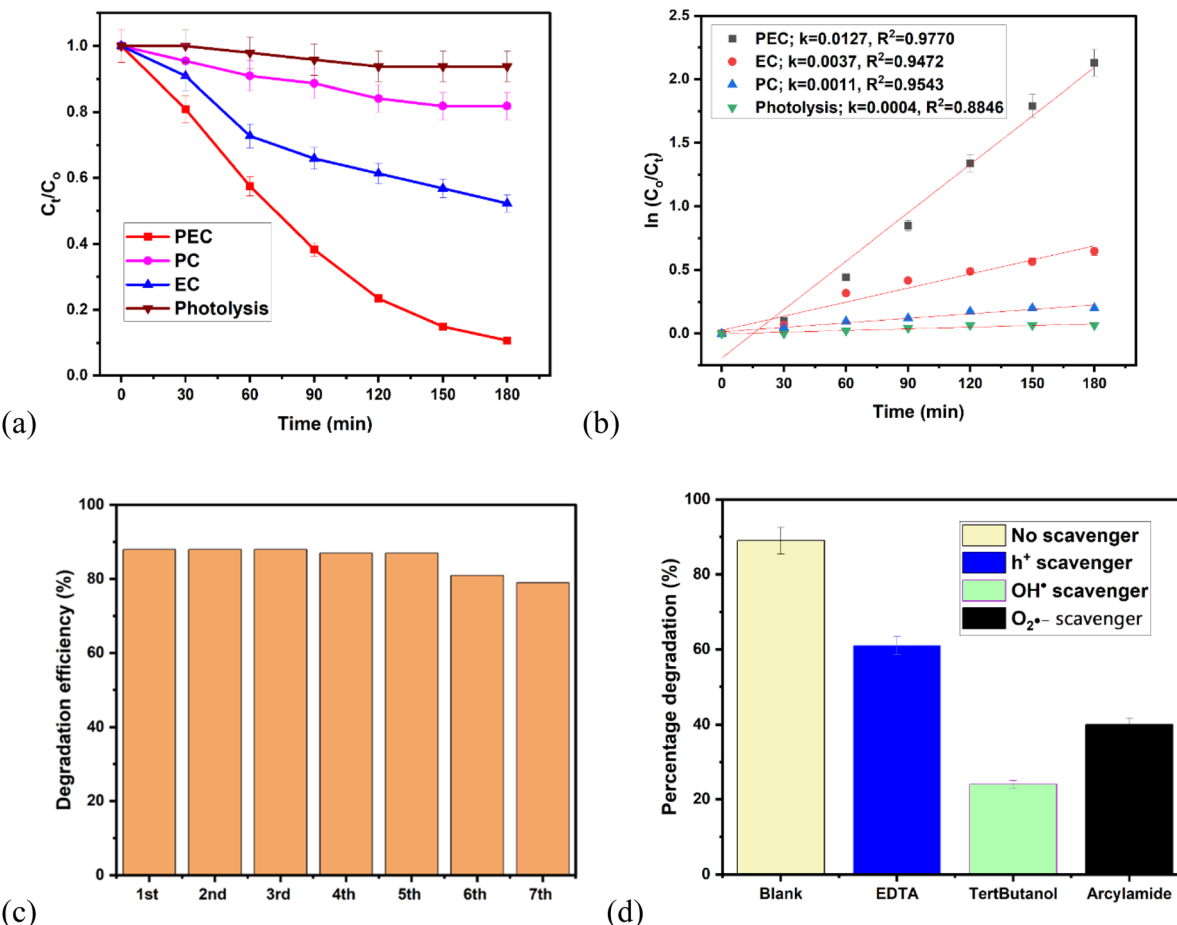


Fig. 5 PEC degradation efficiency plot showing (a) synergistic effect, (b) kinetics study, (c) reusability study. (d) Scavenger study (experimental conditions: ciprofloxacin concentration = 5 mg L⁻¹ in 0.1 M Na₂SO₄, current density = 5 mA cm⁻², pH = 7).

degradation efficiency reduced to 79%. Hence, a reduction of 9% was observed after 7-cycle treatment suggesting that the photoanode is stable. To further investigate the stability of the photoanode, the TEM analysis was conducted after the degradation process. As shown in Fig. S13, no observable changes were noted in the morphology as the observed nanorods and nanosheets were still intact. Furthermore, the BiOBr/Bi₂O₃S photoanode was subjected to XRD analysis after the degradation process. As shown in Fig. S14, all characteristic peaks of BiOBr/Bi₂O₃S remained visible. The additional peaks observed at approximately 28.8° and 36.4° correspond to polyvinylidene fluoride (PVDF)⁵⁶ and fluorine-doped tin oxide (FTO),⁵⁷ respectively, which were used in the electrode fabrication process.

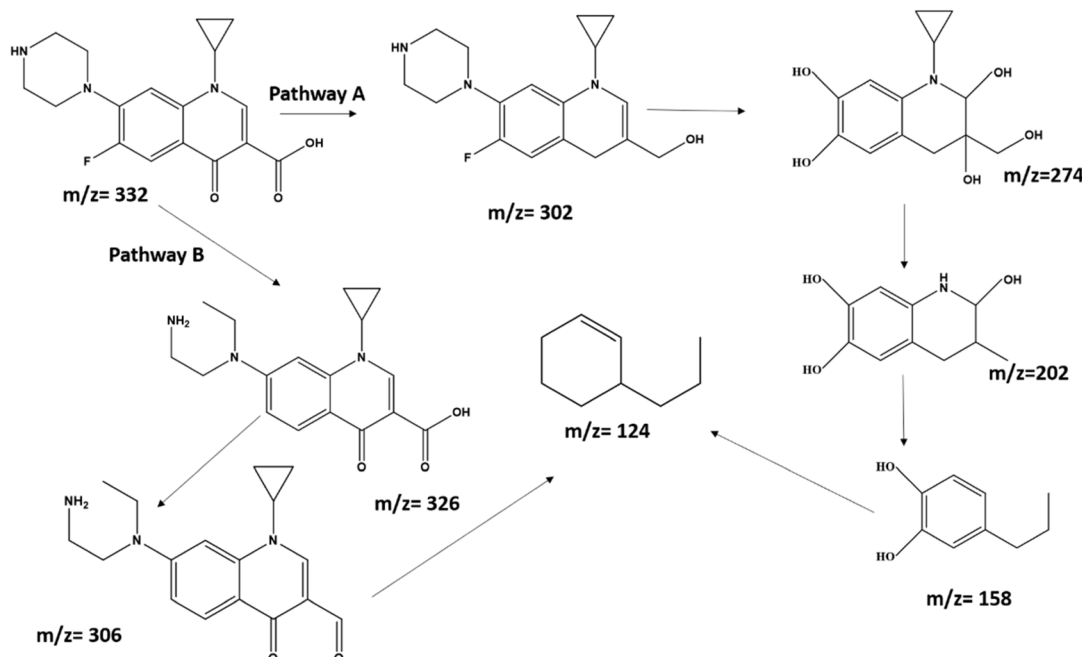
Radical trapping experiment was used to investigate the reactive species that are most responsible for the degradation of ciprofloxacin over BiOBr/Bi₂O₃S photoanode. And, as revealed in Fig. 5d, the degradation efficiency reduced from 88% to 61% when EDTA (hole scavenger)⁵⁸ was added to the solution, while scavenging of hydroxyl radical and superoxide anion radical gave 24% and 40% respectively. The scavenging of reactive species experiment shows that the primary reactive species that contributed to the degradation of ciprofloxacin is the hydroxyl radical followed by the superoxide anion radical which played

a secondary role. However, photogenerated hole also contributed to the degradation process.

3.6. Degradation product and pathways

The PEC oxidation of ciprofloxacin over BiOBr/Bi₂O₃S can lead to the formation of intermediates and by products. UPLC-MS was used to deduce the proposed degradation pathway and products formed. The degradation products were observed to have formed after 1 h degradation process (Fig. S15), with the parent peak of ciprofloxacin at *m/z* 332.14 almost disappearing after. As displayed in Scheme 1, two possible pathways were deduced from the mass to charge ratio (*m/z*) in the spectra. Pathway A suggests that steps involving hydroxyl radical initiated reaction led to dehydroxylation of carbonyl group in (*m/z* 302), then further oxidation led to the cleavage of piperazine ring and hydrolysis (*m/z* 274), followed by the cleavage of the cyclopropyl ring and dehydroxylation (*m/z* 202), deamination then led to pyridine ring opening, demethylation and dehydroxylation, thereby, further oxidative reaction led to the formation of the cycloalkene by-product (*m/z* 124). On the other hand, Pathway B suggests that due to direct hole-initiated oxidation, the piperazine ring in ciprofloxacin was opened, and rearrangement led to the intermediate formed at *m/z* 326,





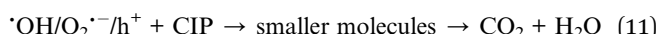
Scheme 1 Proposed pathway and degradation products of ciprofloxacin.

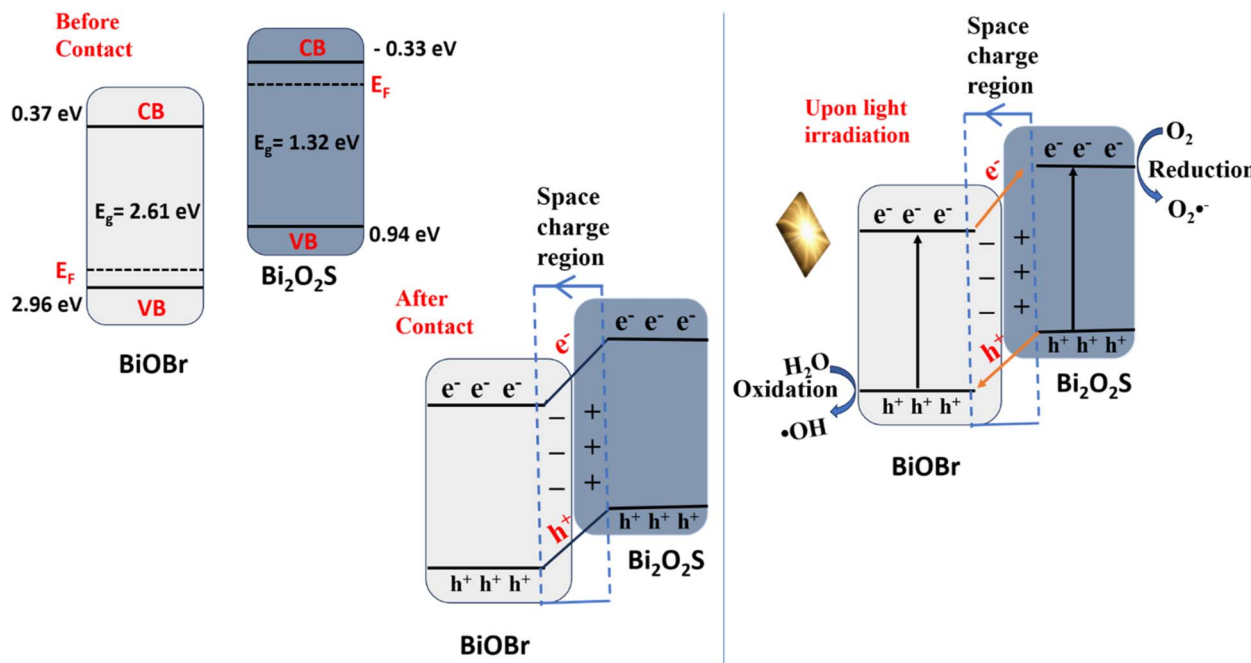
then decarboxylation led to the formation of *m/z* 306 intermediate, which undergo further oxidative cleavage to form the cycloalkene by-product (*m/z* 124). These intermediates and by-product are unstable, and further oxidation can lead to mineralisation to form H_2O and CO_2 .

3.7. Proposed heterojunction formation and mechanism of degradation

The XPS valence analysis and band energy calculations of p-type BiOBr and n-type $\text{Bi}_2\text{O}_2\text{S}$ show a typical type II band alignment in the heterojunction formation. Hence, the charge transfer mechanism in a type II heterojunction formation would suggest that the h^+ in the VB of $\text{Bi}_2\text{O}_2\text{S}$ and the e^- in the CB of BiOBr would take part in the oxidation and reduction processes, leading to the degradation of ciprofloxacin. However, the scavenger studies revealed that the hydroxyl radical and superoxide anion radical play a major role in the degradation of ciprofloxacin, with a minor contribution of photogenerated holes. Therefore, the type II heterojunction model cannot be used to explain the mechanism involved in BiOBr/ $\text{Bi}_2\text{O}_2\text{S}$ heterojunction, because the VB of $\text{Bi}_2\text{O}_2\text{S}$ does not possess sufficient oxidation potential required to oxidise water to generate hydroxyl radical ($\text{·OH}/\text{H}_2\text{O} = +2.27\text{ V}$) and the CB of BiOBr does not possess sufficient reduction potential required to reduced absorbed oxygen to superoxide anion radical ($\text{O}_2/\text{O}_2^{\cdot-} = -0.33\text{ V}$). In addition, the result shows that the preserved photogenerated charge carriers with the highest oxidation and reduction ability were used in the degradation of ciprofloxacin. This makes the charge transfer mechanism involve resemble the Z-scheme heterojunction. However, the XPS analysis shows that the heterojunction formation in BiOBr/ $\text{Bi}_2\text{O}_2\text{S}$ was because of electron redistribution at the interface which led to the

formation of space charge transfer which reveals the charge separation observed by the photoanode. With this evidence, we propose that a p-n junction was formed between the p-type BiOBr and n-type $\text{Bi}_2\text{O}_2\text{S}$ photoanode and it is responsible for the mechanism involved in the reaction. Herein, as displayed in Scheme 2 upon contact between $\text{Bi}_2\text{O}_2\text{S}$ and BiOBr, electrons will flow from $\text{Bi}_2\text{O}_2\text{S}$ (electron-rich) to BiOBr, causing the surface of $\text{Bi}_2\text{O}_2\text{S}$ to be positively charged, and photogenerated holes will migrate from BiOBr (hole rich) to $\text{Bi}_2\text{O}_2\text{S}$, causing the surface of BiOBr to be negatively charged. The redistribution of charges at the interface of BiOBr/ $\text{Bi}_2\text{O}_2\text{S}$ will lead to the formation of space charge region, thus leading to band bending and a built-in electric field, which creates a barrier that reduces the rate of recombination of electron-hole pairs. Upon light irradiation, the photogenerated holes will be drawn to the VB of BiOBr and the photogenerated electrons will be drawn to the CB of $\text{Bi}_2\text{O}_2\text{S}$ where they participate in the pollutant removal process, and eqn (8)–(11) highlight the mechanism involved in the degradation process of ciprofloxacin. The heterojunction design combines the 2D structure of BiOBr and 1D structure of $\text{Bi}_2\text{O}_2\text{S}$ to improve the interfacial contact area and for a p-n heterojunction which led to suppressed recombination rate and promotes the generation of reactive species for the degradation of organic pollutants in water.





Scheme 2 Proposed heterojunction formation of BiOBr/Bi₂O₂S and degradation mechanism.

4. Conclusion

A 2D/1D BiOBr/Bi₂O₂S heterojunction photoanode, with an optimised ratio of 20% Bi₂O₂S was used to degrade organic pollutants in water under visible light irradiation. The structural and electronic synergy, and charge redistribution within the heterojunction improve charge separation, visible light absorption, and generation of reactive species, leading to enhanced PEC degradation of the selected organic pollutants. The radical scavenging experiments highlight the primary role of hydroxyl radicals in the PEC degradation process of ciprofloxacin. The space charge region in the p-n heterojunction supports the proposed mechanism driven by the band alignment and charge redistribution, leading to suppressed recombination rate of the charge carriers. This work provides understanding into the optimisation and applicability of p-n heterojunction for broader environmental remediation applications.

Author contributions

KD Jayeola: conceptualization, methodology, investigation, writing – original draft. DS Sipuka: methodology, writing – review & editing. TI Sebokolodi: methodology, writing – review & editing. JO Babalola: writing – review & editing, supervision. Y Zhao: writing – review & editing. OA Arotiba: methodology, writing – review & editing, supervision, funding acquisition, resources.

Conflicts of interest

There are no conflicts of interest to declare.

Data availability

The data supporting this article have been included as part of the SI. See DOI: <https://doi.org/10.1039/d5ra03795f>.

Acknowledgements

Our appreciation goes to the Centre for Nanomaterials Science Research, University of Johannesburg, South Africa and the National Research Foundation of South Africa (Grant Number CPRR240511218302) for financial support. The authors thank Dr Molahlegi O. Sebabi (Instrument Scientist, Spectrum, Faculty of Science, University of Johannesburg) for running the XRD.

References

- 1 W. Gwenzi and N. Chaukura, *Sci. Total Environ.*, 2018, **619**, 1493–1514.
- 2 A. Mukhopadhyay, S. Duttagupta and A. Mukherjee, *J. Environ. Chem. Eng.*, 2022, **10**, 107560.
- 3 O. A. Arotiba, B. O. Orimolade and B. A. Koiki, *Curr. Opin. Electrochem.*, 2020, **22**, 25–34.
- 4 M. G. Peleyeju and O. A. Arotiba, *Environ. Sci.:Water Res. Technol.*, 2018, **4**, 1389–1411.
- 5 B. A. Koiki, C. Muzenda, K. D. Jayeola, M. Zhou, F. Marken and O. A. Arotiba, *J. Phys. Chem. Lett.*, 2023, **14**, 8880–8889.
- 6 P. Fernandez-Ibanez, S. McMichael, A. Cabanillas, S. Alkharabsheh, A. Moranchel and J. Byrne, *Curr. Opin. Chem. Eng.*, 2021, **34**, 100725.
- 7 X. Zhang, W. Yu, Y. Guo, S. Li, Y. Chen, H. Wang and Z. Bian, *Chem. Eng. J.*, 2023, **455**, 140801.



8 P. Alulema-Pullupaxi, P. J. Espinoza-Montero, C. Sigcha-Pallo, R. Vargas, L. Fernández, J. M. Peralta-Hernandez and J. L. Paz, *Chemosphere*, 2021, **281**, 130821.

9 J. Yu, J. González-Cobos, F. Dappozze, P. Vernoux, A. Caravaca and C. Guillard, *Green Chem.*, 2024, **26**, 1682–1708.

10 Y. Zhao, S. Zhang, R. Shi, G. I. N. Waterhouse, J. Tang and T. Zhang, *Mater. Today*, 2020, **34**, 78–91.

11 B. Luo, G. Liu and L. Wang, *Nanoscale*, 2016, **8**, 6904–6920.

12 L. Meng, Y. Qu and L. Jing, *Chin. Chem. Lett.*, 2021, **32**, 3265–3276.

13 S. E. Jun, J. K. Lee and H. W. Jang, *Energy Adv.*, 2023, **2**, 34–53.

14 K. Wang, Y. Zhang, L. Liu, N. Lu and Z. Zhang, *J. Mater. Sci.*, 2019, **54**, 8426–8435.

15 M. M. Mahdi and S. Esmai, *Int. J. Heat Technol.*, 2024, **42**, 219.

16 S.-Z. Zhao, Y. Lu, R. Lu, Y.-D. Hu, R. D. Rodriguez and J.-J. Chen, *J. Water Process Eng.*, 2023, **54**, 103972.

17 Y. Feng, X. Jiang, L. Sun, J. Meng, N. Jiang and J. Wang, *J. Alloys Compd.*, 2023, **938**, 168698.

18 C. Liu, S. Mao, H. Wang, Y. Wu, F. Wang, M. Xia and Q. Chen, *Chem. Eng. J.*, 2022, **430**, 132806.

19 Z.-Q. Wang, H. Wang, X.-F. Wu and T.-L. Chang, *J. Alloys Compd.*, 2020, **834**, 155025.

20 K. Liu, H. Zhang, Y. Muhammad, T. Fu, R. Tang, Z. Tong and Y. Wang, *Sep. Purif. Technol.*, 2021, **274**, 118992.

21 Y. Ling, Y. Dai and J. Zhou, *J. Colloid Interface Sci.*, 2020, **578**, 326–337.

22 S.-S. Liu, Q.-J. Xing, Y. Chen, M. Zhu, X.-H. Jiang, S.-H. Wu, W. Dai and J.-P. Zou, *ACS Sustain. Chem. Eng.*, 2018, **7**, 1250–1259.

23 K. D. Jayeola, D. S. Sipuka, T. I. Sebokolodi, O. V. Nkwachukwu, C. Muzenda, B. A. Koiki, J. O. Babalola, M. Zhou and O. A. Arotiba, *Chem. Eng. J.*, 2024, **479**, 147482.

24 L. Jiang, Z. Li, D. Wang, T. Guo and Y. Hu, *Appl. Surf. Sci.*, 2022, **601**, 154185.

25 Z. Wu, J. Xie, S. Yin, Z. Lu, J. Hu and Y. Cao, *Chem. Commun.*, 2024, **60**, 8403–8406.

26 J. Hu, A. Al-Salihy, J. Wang, X. Li, Y. Fu, Z. Li, X. Han, B. Song and P. Xu, *Adv. Sci.*, 2021, **8**, 2103314.

27 K. K. Sodhi and D. K. Singh, *J. Water Process Eng.*, 2021, **43**, 102218.

28 S. Bhatt and S. Chatterjee, *Environ. Pollut.*, 2022, **315**, 120440.

29 C. Li, J. Zhang, X. Chen, H. Tao, Y. Zhou and M. Zhu, *Chem. Eng. J.*, 2023, **468**, 143753.

30 L. Zhao, H. Li and L. Wang, *J. Fuel Chem. Technol.*, 2022, **50**, 122–128.

31 T. L. Yusuf, S. A. Ogundare, F. Opoku, O. A. Arotiba and N. Mabuba, *J. Environ. Chem. Eng.*, 2023, **11**, 110711.

32 P. Arunachalam, M. N. Shaddad, M. S. Amer, A. M. Alsalmam and J. Madhavan, *Environ. Sci.: Nano*, 2024, **11**, 2668–2682.

33 B. O. Orimolade, B. A. Koiki, G. M. Peleyeju and O. A. Arotiba, *Electrochim. Acta*, 2019, **307**, 285–292.

34 N. Mahhumane, L. M. Cele, C. Muzenda, O. V. Nkwachukwu, B. A. Koiki and O. A. Arotiba, *Nanomaterials*, 2022, **12**, 2467.

35 H. Wang, R. Bai, Y. Zhang, Z. Han, Y. Zhou and X. Zhao, *Chem. Eng. J.*, 2025, **516**, 164113.

36 X. Zhao, L. Duan, M. Chen, P. Yang, Q. Liu, Y. Liu, H. Zhang, Z. He, G. Hu and Y. Zhou, *Chem. Eng. J.*, 2024, **485**, 149928.

37 M. Petruleviciene, I. Savickaja, J. Kover-Jarosevic, J. Juodkazyte, A. Padarauskas, A. Griguceviciene and A. Ramanavicius, *ACS Omega*, 2025, **10**, 8538–8550.

38 S. Rani, V. Gopal, H. P. Reddy and A. Selvaraj, *Chem. Eng. J.*, 2025, **516**, 164063.

39 J. Xu, Y. Wang, J. Niu and M. Chen, *Sep. Purif. Technol.*, 2019, **225**, 24–32.

40 D. C. Akintayo, T. L. Yusuf and N. Mabuba, *Colloids Surf., A*, 2025, **721**, 137215.

41 B. Ma, S. Xin, X. Ma, C. Zhang and M. Gao, *Appl. Surf. Sci.*, 2021, **551**, 149480.

42 C. Dong, Z. Zheng, M. A. H. Badsha, J. He and I. M. C. Lo, *Environ. Int.*, 2021, **154**, 106572.

43 M. Cai, B. Du, A. Shui and C. He, *Appl. Surf. Sci.*, 2023, **612**, 155807.

44 L. Mao, H. Liu, L. Yao, W. Wen, M.-M. Chen, X. Zhang and S. Wang, *Chem. Eng. J.*, 2022, **429**, 132297.

45 K. D. Jayeola, D. S. Sipuka, T. I. Sebokolodi, J. O. Babalola, M. Zhou, F. Marken and O. A. Arotiba, *ACS Appl. Mater. Interfaces*, 2025, **17**, 1385–1398.

46 L. Li, M. A. Boda, C. Chen, F. Wang, Y. Liu and Z. Yi, *Cryst. Growth Des.*, 2021, **21**, 7179–7185.

47 X. Geng, W. Li, F. Xiao, D. Wang and L. Yang, *Catal. Sci. Technol.*, 2017, **7**, 658–667.

48 K. D. Jayeola, D. S. Sipuka, T. I. Sebokolodi, O. V. Nkwachukwu, C. Muzenda, B. A. Koiki, J. O. Babalola, M. Zhou and O. A. Arotiba, *Electrochim. Acta*, 2024, 145160.

49 C. Niu, T. Zhu and Y. Lv, *Int. J. Photoenergy*, 2019, **2019**, 1476217.

50 P. Singh, Sonu, P. Raizada, A. Sudhaik, P. Shandilya, P. Thakur, S. Agarwal and V. K. Gupta, *J. Saudi Chem. Soc.*, 2019, **23**, 586–599.

51 N. Luhakhra and S. K. Tiwari, *Colloids Surf., A*, 2023, **677**, 132332.

52 O. C. Olatunde, T. L. Yusuf, N. Mabuba, D. C. Onwudiwe and S. Makgato, *J. Water Process Eng.*, 2024, **59**, 105074.

53 A. P. Chowdhury and B. H. Shambharkar, *Chem. Eng. J. Adv.*, 2020, **4**, 100040.

54 Y. Li, J. Ma, L. Xu, T. Liu, T. Xiao, D. Chen, Z. Song, J. Qiu and Y. Zhang, *Adv. Sci.*, 2023, **10**, 2207514.

55 M. Dimpe and P. Nomngongo, *J. Pharm. Anal.*, 2019, **9**, 117–126.

56 I. Abdullah, M. Hj. Jumali, M. Yahaya and H. Shanshool, *Adv. Environ. Biol.*, 2015, **9**(20), 20–27.

57 S. Guan, A. Mori, M. Kato and X. Zhao, *J. Mater. Sci.: Mater. Electron.*, 2020, **31**, 9982–9988.

58 C. Chu, Y. Qin, C. Ni, N. Wu and J. Zou, *Appl. Catal., B*, 2024, **341**, 123321.

